Nat. Hazards Earth Syst. Sci. Discuss., 3, 1291–1328, 2015
www.nat-hazards-earth-syst-sci-discuss.net/3/1291/2015/
doi:10.5194/nhessd-3-1291-2015

Natural Hazards and Earth System Sciences
Open Access
Discussions

Three dimensional slope stability problem with a surcharge load

Y. M. Cheng[1], N. Li[1], and X. Q. Yang[2]

[1]Department of Civil and Environmental Engineering, Hong Kong Polytechnic University, Hong Kong, China
[2]Building and Construction Department, Guangdong University of Technology, Guangzhou, China

Received: 15 January 2015 – Accepted: 25 January 2015 – Published: 11 February 2015

Correspondence to: Y. M. Cheng (ceymchen@poly.edu.hk)

Published by Copernicus Publications on behalf of the European Geosciences Union.

Abstract

An analytical solution for the three dimensional stability analysis of the ultimate uniform patched load on top of a slope is developed by the limit analysis using kinematically admissible failure mechanisms. The failure mechanism which is assumed in the analytical solution is verified by three-dimensional strength reduction analyses and laboratory model test. Furthermore, the proposed method and the results are further compared with some published results for illustrating the applicability of the proposed failure mechanism.

1 Introduction

Many practical geotechnical problems are three dimensional in nature, yet two-dimensional plane-strain analysis is commonly used for simplicity of analysis. This pertain to problems as natural slopes, cut slopes and fill slopes for which the failure regions usually have finite dimensions, and the actual problems are far from the plane strain condition. For two-dimensional slope stability by the limit equilibrium method, the factor of safety is based on the equilibrium of discrete slices (Bishop, 1955; Morgenstern and Price, 1965; Spencer, 1967; Janbu, 1973). Two dimensional analyses, though helpful for designing most of the slopes and embankments, are conservative and are not applicable to slopes with finite widths or with local loads. Cheng et al. (2007) has demonstrated that the strength reduction method is similar to the limit equilibrium method in most cases, and the strength reduction method will also be adopted for comparisons in this study.

The common approach to the three-dimensional slope stability analysis is the limit-equilibrium methods which are direct extensions of the corresponding two-dimensional methods (Hovland,1977; Chen and Chameau, 1982; Azzouz and Baligh, 1983; Hungr, 1987; Lam and Fredlund, 1993; Huang and Tsai, 2000, 2002). There are also several three-dimensional limit analysis models (Giger and Krizek, 1975; Michalowski, 1989;

Chen et al., 2001a, b; Farzaneh and Askari, 2003) in literature. Michalowski (1989), Chen et al. (2001a, b) and Farzaneh and Askari (2003) have considered the three-dimensional problem by the limit analysis and the upper-bound theorem of plasticity, which are based on the three-dimensional models by Chen (1975). Cheng and Yip (2007) have proposed a three-dimensional limit equilibrium (LEM) slope stability model with explicit consideration of the sliding direction, and Wei and Cheng (2009) have carried out a detailed study about three-dimensional slope stability analysis using strength reduction method (SRM). The safety factor for a three-dimensional problem is defined in the same way as for the corresponding two-dimensional problems:

$$c_e = c/k \tag{1}$$

$$\tan\varphi_e = \tan\varphi/k \tag{2}$$

where c and φ are soil cohesion strength and internal friction angle, k is the traditional safety factor, c_e and φ_e are the mobilized cohesive strength and internal friction angle which will be denoted as c and φ in the later part of this paper for simplicity. In most of the previous works based on the limit analysis, the failure mass is divided into several blocks with velocity discontinuity planes and energy balance is applied (Chen, 1975). This approach is acceptable for a two-dimensional analysis, but a realistic three-dimensional failure mechanism should have a radial shear zone which is difficult to be modeled by wedges. Chen et al. (2003) overcome this limitation by the use of many small rigid elements and nonlinear programming technique for the minimization analysis, but this method requires very long computer time in the optimization process and the location of the global minimum is not easily achieved.

In this paper, the analytical solutions for a patched uniform distributed load acting on or below the top surface of a slope are developed. This problem can also be viewed as a bearing capacity problem as well as a slope stability problem. The failure mechanism presented in this study is a more reasonable mechanism based on the kinematically admissible approach of a typical bearing capacity problem. It is a further development of the works based on some of the above researches by using a more reasonable three-dimensional radial shear failure zone through which other three dimensional failure wedges are connected together with, and a solution can be obtained within very short time as the analytical expressions are available. The present solutions have given good solutions when compared with some previous studies and a laboratory test. The laboratory test has also revealed some interesting progressive failure phenomenon and deformation characteristic for this slope failure problem.

Kinematically admissible velocity fields used in the upper bounds analysis usually have a distinct physical interpretation which is associated with the true collapse mechanisms known from experiments and practical experience. The present failure mechanism complies with the requirements in limit analysis and is similar to that as found from laboratory tests which will be illustrated in a later section. Stress fields used in the lower-bound approach, however, are constructed without a clear relation to the real stress fields, other than the stress boundary conditions. Moreover, most problems involve a semi-infinite half-space and the extension of the stress field into the half-space is either cumbersome or appears to be impossible (Michalowski, 1989). For general three-dimensional problems, the construction of an admissible stress field is very difficult, and only very few cases are successfully solved by the lower bound approach. As a result, only the upper-bound kinematical admissible approach is commonly adopted for solving such type of problems. As demonstrated by Cheng et al. (2013), under the action of self weight, the classical log-spiral zone is no longer a rigorous solution to the failure mechanism. For a sloping ground, the authors have tried the slip-line analysis and have found that the classical log-spiral and wedge failure mechanism will enclose the slip-line solution (but very close), which means that the volume of failure mass from plasticity formulation is only slightly less than that from the classical formulation using log-spiral curve.

NHESSD
3, 1291–1328, 2015

2 Three-dimensional slope failure of a slope with patched load on the top surface ($D = 0$ m)

A simple three-dimensional slope failure mechanism with zero embedment depth patch load ($D = 0$ m) is shown in Fig. 1. The surface between the footing and the soil is assumed to be smooth in the present study. Figure 1b is the failure mechanism at the section through the applied load, while the end effects are shown in Fig. 1c and the bird view of the three-dimensional failure mechanism is shown in Fig. 1d. The total works done are calculated as below.

2.1 Rate of work done produced along load length L

Based on Fig. 1b, the resistance rate of work done P dissipated by the cohesion c along the velocity discontinuity plane $ac \cdot L$ is given as:

$$P_{R1} = c \cdot ac \cdot L \cdot v_0 \cos\varphi \tag{3}$$

where $ac = B\sin\xi / \sin(\zeta + \xi)$ and $r_0 = bc = B\sin\zeta / \sin(\zeta + \xi)$, B is the width of the footing and L is the length of the footing normal to the section as shown in Fig. 1b but excluding the two end effects. Resistance rate of work done dissipated in the radial shear zone bcd is written as:

$$P_{R2} = cv_0r_0L\frac{\exp(2\Theta\tan\varphi) - 1}{\tan\varphi} \tag{4}$$

Resistance rate of work done dissipated by cohesion c along the velocity discontinuity plane $dg \cdot L$ is given by:

$$P_{R3} = c \cdot dg \cdot L \cdot v_3 \cos\varphi \tag{5}$$

in which $v_3 = v_0\exp(\Theta\tan\varphi)$, and $bd = r_0\exp(\Theta\tan\varphi)$.

As shown in Fig. 1b, point b is taken as the reference point (0,0,0) of the coordinates axes, and positive directions are pointing towards left and downward. If the coordinate

NHESSD
3, 1291–1328, 2015

Y. M. Cheng et al.

of point b is $x_b = 0$, $y_b = 0$, $z_b = 0$, the corresponding coordinate of point i is $x_i = b$, $y_i = 0$, $z_i = 0$, coordinate of point d is $x_d = bd\cos\eta$, $y_d = 0$, $z_d = bd\sin\eta$. To obtain the values x_g and z_g, the following geometric relationships are established and used:

$$\frac{z_g - z_d}{x_g - x_d} = \tan(\varphi + \eta - 90°), \quad \text{and} \quad \frac{z_g - z_i}{x_g - x_i} = \tan\beta \tag{6}$$

Based on Eq. (6), x_g and z_g are expressed as:

$$x_g = \frac{b\tan\beta + z_d - x_d\tan(\varphi + \eta - 90°)}{\tan\beta - \tan(\varphi + \eta - 90°)}, \quad \text{and} \quad z_g = (x_g - b)\tan\beta \tag{7}$$

and dg in Eq. (5) is obtained as:

$$dg = \sqrt{(x_g - x_d)^2 + (z_g - z_d)^2} \tag{8}$$

The rate of work done produced by the external pressure q on the top of the slope is expressed as:

$$P_{\mathrm{D1}} = qBLv_1 \tag{9}$$

The rate of work done produced by the weight of the wedge abc is written as:

$$P_{\mathrm{D2}} = W_{abc}v_0\sin(\zeta - \varphi) \tag{10}$$

where $W_{abc} = \frac{\gamma}{2}ac\cdot B\cdot L\sin\zeta$. The rate of work done produced by the weight of the radial shear zone bcd is given as:

$$\begin{aligned} P_{\mathrm{D3}} &= \frac{\gamma}{2}\int_0^{\Theta} r^2 Lv\cos(\theta + \xi)\mathrm{d}\theta \\ &= \frac{\gamma}{2}r_0^2 Lv_0\frac{\exp(3\Theta\tan\varphi)[\sin(\Theta + \xi) + 3\tan\varphi\cos(\Theta + \xi)] - \sin\xi - 3\tan\varphi\cos\xi}{1 + 9\tan^2\varphi} \end{aligned} \tag{11}$$

NHESSD
3, 1291–1328, 2015

Three dimensional slope stability problem

Y. M. Cheng et al.

The rate of work done dissipated by the weight of the wedge $bdgi$ is formulated as:

$$P_{D4} = W_{bdgi} \cdot v_3 \cos(180^\circ - \eta) \tag{12}$$

$$W_{bdgi} = \gamma L (S_{big} + S_{bdg}) \tag{13}$$

where $S_{bdg} = \frac{1}{2} bd \cdot dg \cos\varphi$, and $S_{big} = \frac{1}{2} bi \cdot gi \sin\beta$, in which $bi = b$, and $gi = \sqrt{(x_g - x_i)^2 + (z_g - z_i)^2}$.

2.2 Rate of work done produced at the two end failure zones of the footing

1. End failure zone 1
   As shown in Fig. 1c, cc' is a horizontal line normal to the plane abc. In order to ensure that the sliding velocity of the soil mass of the end-failure zone 1 is equal to v_0, the angle between ac and should be equal to φ, therefore, $cc' = r_0 \tan\varphi$, $r_0 = ac$. The rate of work done by the velocity discontinuity plane acc' is then expressed as

   $$P_{RE1} = c \cdot S_{acc'} \cdot v_0 \cos\varphi \tag{14}$$

   where $S_{acc'} = \frac{1}{2} ac \cdot cc'$. The rate of work done produced by the weight of the wedge $abc - c'$ is expressed as:

   $$P_{DE1} = W_{abc-c'} \cdot v_0 \sin(\zeta - \varphi) \tag{15}$$

   in which $ab = B$, $S_{abc} = \frac{1}{2} ab \cdot ac \sin\zeta, W_{abc-c'} = \frac{\gamma}{3} S_{abc} \cdot cc'$.

2. End failure zone 2
   As shown in Fig. 1c, $b - cdd'c'$ is the three-dimensional end radial shear failure zone 2. If we assume that $c'd'$ is a spiral and the center of the spiral $c'd'$ is at point b, a relationship $R = R_0 \exp(\varepsilon \tan\varphi)$ will exist in which $R_0 = bc'$ and $R =$

NHESSD
3, 1291–1328, 2015

bf'. For triangle bff', the velocity v is normal to both lines bf and bf', so we can deduce that the velocity v is vertical to triangle bff' and line ff'. In order to ensure kinematically compatible velocity yield for the soil mass of the end radial shear failure zone 2, for small unit $b-fkk'f'$, the horizontal angle between $v = v_0 \exp(\theta \tan\varphi)$ and line $f'k'$ should be equal to φ. It should be pointed out that $cc'd'd$ is normal to the plane abc, and the corresponding relationship between $Rd\varepsilon$ and $rd\theta$ is expressed as:

$$rd\theta/\cos\varphi = Rd\varepsilon \tag{16}$$

in which $r = r_0 \exp(\theta\tan\varphi)$, $R = R_0 \exp(\varepsilon\tan\varphi)$, and $r_0 = R_0 \cos\varphi$. Integrating both sides of Eq. (16) yield:

$$\theta = \varepsilon, \quad \Theta = \varepsilon_H \tag{17}$$

in which Θ is an angle between bc and bd, and ε_H is the angle between line bc' and line bd'.

(a) Velocity discontinuity curve plane $bc'd'$

Velocity discontinuity plane area bfk' is expressed as:

$$S_{bf'k'} = \frac{1}{2}R^2 \sin d\varepsilon = \frac{1}{2}R^2 d\varepsilon \tag{18}$$

Therefore the resistance rate of work done produced by c along the velocity discontinuity plane $bc'd'$ is integrated as:

$$\begin{aligned} P_{\mathrm{RE2}} &= \int_0^{\varepsilon_H} c \cdot S_{bf'k'} \cdot v\cos\varphi = \frac{1}{2} c v_0 R_0^2 \cos\varphi \int_0^{\Theta} \exp(3\theta\tan\varphi)\mathrm{d}\theta \\ &= \frac{\cos\varphi}{6\tan\varphi} c v_0 R_0^2 [\exp(3\Theta\tan\varphi) - 1] \end{aligned} \tag{19}$$

NHESSD
3, 1291–1328, 2015

Three dimensional slope stability problem

Y. M. Cheng et al.

(b) Velocity discontinuity plane $cc'd'd$

Line ff' is normal to line bf, therefore ff' is expressed as:

$$ff' = (R^2 - r^2)^{\frac{1}{2}} = r_0 \tan\varphi \exp(\theta \tan\varphi) \tag{20}$$

Unit area of $ff'k'k$ is expressed as:

$$S_{ff'k'k} = ff' \cdot R d\varepsilon = r_0 R_0 \tan\varphi \exp(2\theta \tan\varphi) \mathrm{d}\theta \tag{21}$$

Therefore, the resistance rate of work done produced by the velocity discontinuity area $cc'd'd$ is obtained as:

$$P_{\mathrm{RE3}} = \int_0^{\Theta} S_{ff'k'k} \cdot v \cdot c \cos\varphi = \frac{1}{3} r_0^2 v_0 c[\exp(3\Theta \tan\varphi) - 1] \tag{22}$$

(c) Radial shear zone $b - cc'd'd$

Area of triangle bff' is expressed as:

$$S_{bff'} = \frac{1}{2} bf \cdot ff' = \frac{1}{2} r_0^2 \tan\varphi \exp(2\theta \tan\varphi) \tag{23}$$

in which $bf = r_0 \exp(\theta \tan\varphi)$. Dissipated rate of work done produced in the radial zone is given as:

$$P_{\mathrm{RE4}} = \int_0^{\Theta} S_{bff'} \cdot c \cdot v \mathrm{d}\theta = \frac{1}{2} r_0^2 c v_0 \tan\varphi \int_0^{\Theta} \exp(3\theta \tan\varphi) \mathrm{d}\theta$$
$$= \frac{1}{6} r_0^2 c v_0 [\exp(3\Theta \tan\varphi) - 1] \tag{24}$$

NHESSD
3, 1291–1328, 2015

(d) Weight of the radial zone $b-cc'd'd(0 \le \theta \le \Theta)$
The weight of the unit wedge $b-ff'kk'$ is obtained as:

$$W_{b-ff'k'k} = \frac{\gamma}{3} S_{ff'k'k} \cdot bf \cos\varphi = \frac{\gamma}{3} r_0^2 R_0 \sin\varphi \exp(3\theta \tan\varphi) d\theta \quad (25)$$

Therefore the driving rate of work done produced by the weight of the wedge is expressed as:

$$P_{DE2} = \int_0^{\Theta} W_{b-ff'k'k} \cdot v \cos(\xi + \theta)$$
$$= \frac{\gamma}{3} r_0^2 R_0 v_0 \sin\varphi \frac{\exp[4\Theta \tan\varphi][\sin(\Theta+\xi) + 4\tan\varphi\cos(\Theta+\xi)] - \sin\xi - 4\tan\varphi\cos\xi}{1+16\tan^2\varphi} \quad (26)$$

3. End failure zone 3
As shown in Fig. 1c, line dg is parallel to line $d'g''$. In order to ensure that the kinematical velocity of soil mass of the end failure zone 3 is compatible, the angle between line $d'g'$ and line $d'g''$ should be equal to φ. It should be mentioned that straight lines $gg''g'$ and ii' are both in the slope surface, both triangle $bd'g'$ and triangle $bg'i'$ are located on the same velocity discontinuity plane $bd'g'i'b$, and triangle bii' is located in the top surface of the slope.

(a) Velocity discontinuity plane $dd'g'g$.
The area of velocity discontinuity plane $dd'g'g$ is expressed as:

$$S_{dd'g'g} = dd' \cdot dg + \frac{1}{2} dg \cdot dg \cdot \tan\varphi \quad (27)$$

in which $dd' = r_0 \tan\varphi \exp(\Theta \tan\varphi)$. Resistance rate of work done produced by c along the velocity discontinuity plane is then obtained as:

$$P_{\mathrm{RE5}} = c \cdot S_{dd'g'g} \cdot v_3 \cos\varphi \tag{28}$$

(b) Velocity discontinuity plane $bd'g'i'$

As shown in Fig. 1c, coordinate of point d' is $x_{d'} = x_d, y_{d'} = dd', z_{d'} = z_d$, coordinate of point g' is $x_{g'} = x_g, y_{g'} = dd' + dg \cdot \tan\varphi, z_{g'} = z_g$, and coordinate of i' is $x_{i'} = x_i, y_{i'} = y_i, z_{i'} = z_i$. The equation of the plane formed by points b, d' and g' is written as:

$$\begin{vmatrix} x - x_b & y - y_b & z - z_b \\ x_{d'} - x_b & y_{d'} - y_b & z_{d'} - z_b \\ x_{g'} - x_b & y_{g'} - y_b & z_{g'} - z_b \end{vmatrix} = 0 \tag{29}$$

As point i' should be on the velocity discontinuity plane $bd'g'i'$, x, y, z are replaced by $x_{i'}, y_{i'}, z_{i'}$ in Eq. (29), then $y_{i'}$ is given as:

$$y_{i'} = b \frac{z_{d'} \cdot y_{g'} - y_{d'} \cdot z_{g'}}{z_{d'} \cdot x_{g'} - x_{d'} \cdot z_{g'}} \tag{30}$$

The area of the velocity discontinuity plane $bd'g'$ is expressed as:

$$S_{bd'g'} = \sqrt{\frac{1}{16}(bd' + d'g' + bg')(bd' + d'g' - bg')(bd' - d'g' + bg')(-bd' + d'g' + bg')} \tag{31}$$

in which corresponding $bd' = R_0 \exp(\Theta \tan\varphi), d'g' = dg/\cos\varphi$ and $bg' = \sqrt{(x_b - x_{g'})^2 + (y_b - y_{g'})^2 + (z_b - z_{g'})^2}$.

NHESSD
3, 1291–1328, 2015

The area of the velocity discontinuity plane $bg'i'$ is written as:

$$S_{bg'i'} = \sqrt{\frac{1}{16}(bg'+bi'+g'i')(bg'+bi'-g'i')(bg'-bi'+g'i')(-bg'+bi'+g'i')} \tag{32}$$

where $g'i' = \sqrt{(x_{i'}-x_{g'})^2+(y_{i'}-y_{g'})^2+(z_{i'}-z_{g'})^2}$, and $bi' = \sqrt{b^2+y_{i'}^2}$.

The resistance rate of work done produced by c along the velocity discontinuity plane is written as:

$$P_{\mathrm{RE6}} = c\cdot(S_{bd'g'}+S_{bg'i'})\cdot v_3\cos\varphi \tag{33}$$

(c) Wedge $b-dd'g'g$

Weight of the wedge $b-dd'g'g$ is expressed as

$$W_{b-dd'g'g} = \frac{\gamma}{3}S_{dd'g'g}\cdot bd\cos\varphi \tag{34}$$

The corresponding resistance rate of work done produced by the weight of wedge is obtained as:

$$P_{\mathrm{DE3}} = W_{b-dd'g'g}\cdot v_3\cos(180^\circ-\eta) \tag{35}$$

(d) Wedge $b-gg'i'i$

Weight of the wedge $b-gg'i'i$ is given by:

$$W_{b-gg'i'i} = \frac{\gamma}{3}\cdot S_{gg'i'i}\cdot b\sin\beta \tag{36}$$

in which $S_{gg'i'i} = \frac{1}{2}gi\cdot(y_{i'}+y_{g'})$, $gi = \sqrt{(x_g-x_i)^2+(z_g-z_i)^2}$.

NHESSD
3, 1291–1328, 2015

Then resistance rate of work done produced by the weight of the wedge is:

$$P_{\mathrm{DE4}} = W_{b-gg'i'i} \cdot v_3 \cos(180^\circ - \eta) \tag{37}$$

The total resistance rate of work done of the failure mechanism shown in Fig. 1 is expressed as:

$$P_{\mathrm{R}} = P_{\mathrm{R1}} + P_{\mathrm{R2}} + P_{\mathrm{R3}} + 2\left(P_{\mathrm{RE1}} + P_{\mathrm{RE2}} + P_{\mathrm{RE3}} + P_{\mathrm{RE4}} + P_{\mathrm{RE5}} + P_{\mathrm{RE6}}\right) \tag{38}$$

The total driving rate of work done is obtained as:

$$P_{\mathrm{D}} = P_{\mathrm{D1}} + P_{\mathrm{D2}} + P_{\mathrm{D3}} + P_{\mathrm{D4}} + 2\left(P_{\mathrm{DE1}} + P_{\mathrm{DE2}} + P_{\mathrm{DE3}} + P_{\mathrm{DE4}}\right) \tag{39}$$

By means of Eqs. (1) and (2), the safety factor k are obtained by means of a simple looping method until the following equation is satisfied:

$$P_{\mathrm{R}} - P_{\mathrm{D}} = f(\zeta, \xi, \eta) = 0 \tag{40}$$

Where the angles ζ, ξ and η related to the k value are the critical failure angles, ζ_{cr}, ξ_{cr} and η_{cr}. During the solution of nonlinear equation (40), it is found that the solution is very sensitive to the parameters near to the critical solution. A small change of even 0.5° can sometimes have a noticeable effect to the solution of Eq. (40) under such condition. In views of that, a small interval of 0.2° is chosen in the present study. Even with such a small interval in the search for the critical solution, the solution time is extremely fast and is acceptable.

3 Three-dimensional slope failure with an embedded patched load ($D > 0$ m)

General three-dimensional slope failure with an embedded patch load with $D > 0$ m is shown in Fig. 2. The rates of work done for various components are formulated as below.

NHESSD
3, 1291–1328, 2015

3.1 Rate of work done produced along footing length L

(a) Resistance rate of work done dissipated by cohesion c along velocity discontinuity plane $dg \cdot L$ is calculated by:

$$P_{R3} = c \cdot dg \cdot L \cdot v_3 \cos\varphi \tag{41}$$

in which $v_3 = v_0 \exp(\Theta \tan\varphi)$, and $bd = r_0 \exp(\Theta \tan\varphi)$. As shown in Fig. 2a, if the coordinate of point b is $x_b = 0$, $y_b = 0$, $z_b = 0$, the corresponding coordinate of point i will be $x_i = b, y_i = 0, z_i = -D$, coordinate of point d is $x_d = bd \cos\eta, y_d = 0$, $z_d = bd \sin\eta$, coordinate of point h is $x_h = 0$, $y_h = 0$, $z_h = -D$. The values of x_g and z_g are obtained through the geometric relationships:

$$\frac{z_g - z_d}{x_g - x_d} = \tan(\varphi + \eta - 90°), \quad \text{and} \quad \frac{z_g - z_i}{x_g - x_i} = \tan\beta \tag{42}$$

Based on Eq. (42), x_g and z_g are expressed as:

$$x_g = \frac{b\tan\beta + D + z_d - x_d \tan(\varphi + \eta - 90°)}{\tan\beta - \tan(\varphi + \eta - 90°)}, \quad z_g = (x_g - b)\tan\beta - D \tag{43}$$

And dg in Eq. (41) is obtained as:

$$dg = \sqrt{(x_g - x_d)^2 + (z_g - z_d)^2} \tag{44}$$

(b) Resistance rate of work done produced by the weight of the wedge $bdgih$ Area of $bdgih$ is obtained as:

$$S_{bdgih} = S_{bdg} + S_{big} + S_{bhi} \tag{45}$$

NHESSD
3, 1291–1328, 2015

in which

$$S_{bdg} = \frac{1}{2} bd \cdot dg \cos\varphi \tag{46}$$

$$S_{big} = \sqrt{\frac{1}{16}(bg+gi+bi)(bg+gi-bi)(bg-gi+bi)(-bg+gi+bi)} \tag{47}$$

where $bg = \sqrt{(x_b - x_g)^2 + (z_b - z_g)^2}$, $gi = \sqrt{(x_g - x_i)^2 + (z_g - z_i)^2}$ and $bi = \sqrt{(x_b - x_i)^2 + (z_b - z_i)^2}$

Weight of the wedge $bdgih$ is expressed as:

$$W_{bdgih} = \gamma \cdot L \cdot S_{bdgih} \tag{48}$$

Then, the rate of work done produced by the weight of the wedge $bdgih$ is given as:

$$P_{\mathrm{D4}} = W_{bdgih} \cdot v_3 \cos(180^\circ - \eta) \tag{49}$$

Other items such as P_{R1}, P_{R2} and $P_{\mathrm{D1}} \sim P_{\mathrm{D3}}$ are similar to those given in the previous section and will not be repeated here.

3.2 Rate of work done produced at two failure ends of the buried load

As shown in Fig. 2b, the coordinates of point d', g' and i' are similar to the case of $D = 0$. As point i' should be on the velocity discontinuity plane $bd'g'i'$, x, y, z are replaced by $x_{i'}$, $y_{i'}$, $z_{i'}$ in the Eq. (29), then $y_{i'}$ is:

$$y_{i'} = b\frac{z_{d'} \cdot y_{g'} - y_{d'} \cdot z_{g'}}{z_{d'} \cdot x_{g'} - x_{d'} \cdot z_{g'}} + D\frac{x_{d'} \cdot y_{g'} - y_{d'} \cdot x_{g'}}{z_{d'} \cdot x_{g'} - x_{d'} \cdot z_{g'}} \tag{50}$$

NHESSD
3, 1291–1328, 2015

Three dimensional slope stability problem

Y. M. Cheng et al.

(a) Velocity discontinuity plane $bd'g'i'$.
For the velocity discontinuity plane $bd'g'$, it is similar to the previous case except that

$$bi' = \sqrt{x_{i'}^2 + y_{i'}^2 + z_{i'}^2} \tag{51}$$

The resistance rate of work done produced by c along the velocity discontinuity plane $bd'g'i'$ is also given by Eq. (33).

(b) Resistance rate of work done produced by the tensile failure plane bhi'
Area of the tensile failure plane bhi' is expressed as:

$$S_{bhi'} = \frac{1}{2} D \cdot hi' \tag{52}$$

in which $hi' = \sqrt{b^2 + y_{i'}^2}$. Usually, the tensile strength of soil mass can be taken as $(1/4 \sim 1.0)c$ (Baker, 1981; Bagge, 1985). Calculation as shown in later part of this paper will demonstrate that the tensile strength of soil mass has only a small effect on the safety factor, so it is assumed to be equal to $c/3$ in the present study (any other value can be obtained easily by a very simple modification of Eq. 53). As the tensile direction is along the direction of velocity v_3, the corresponding resistance rate of work done produced by the tensile failure plane is written as:

$$P_{\mathrm{RE7}} = c \cdot S_{bhi'} \cdot v_3/3 \tag{53}$$

(c) Driving rate of work done produced by wedges $b-dd'g'g$, $b-ii'g'g$ and $b-hii'$
Weight of the wedge $b-dd'g'g$ is expressed as:

$$W_{b-dd'g'g} = \frac{\gamma}{3} S_{dd'g'g} \cdot bd \cos\varphi \tag{54}$$

Area of the slope surface $ii'g'g$ is expressed as:

$$S_{ii'g'g} = \frac{1}{2}(ii' + gg') \cdot gi \tag{55}$$

in which $ii' = y_{i'}$, $gg' = dd' + dg\tan\varphi$, and $gi = \sqrt{(x_g - x_i)^2 + (z_g - z_i)^2}$.

Weight of the wedge $b - ii'g'g$ is given as

$$W_{b-ii'g'g} = \frac{\gamma}{3} \cdot S_{ii'g'g} \cdot (b \cdot \sin\beta + D \cdot \cos\beta) \tag{56}$$

Area of triangle hii' is given as:

$$S_{hii'} = \frac{1}{2} b \cdot y_{i'} \tag{57}$$

Weight of the wedge $b - hii'$ is written as:

$$W_{b-hii'i} = \frac{\gamma}{3} \cdot S_{hii'} \cdot D \tag{58}$$

Then driving rate of work done produced by the weight of these wedge is expressed as:

$$P_{\mathrm{DE3}} = (W_{b-dd'g'gi} + W_{b-ii'g'g} + W_{b-hii'}) \cdot v_3 \cos(180^\circ - \eta) \tag{59}$$

Other items $P_{\mathrm{RE1}} \sim P_{\mathrm{RE5}}$ and $P_{\mathrm{DE1}} \sim P_{\mathrm{DE2}}$ are similar to the case for $D = 0$ m and will not be repeated here. Referring to Fig. 2, the total resistance rate of work done is expressed as:

$$P_{\mathrm{R}} = P_{\mathrm{R1}} + P_{\mathrm{R2}} + P_{\mathrm{R3}} + 2(P_{\mathrm{RE1}} + P_{\mathrm{RE2}} + P_{\mathrm{RE3}} + P_{\mathrm{RE4}} + P_{\mathrm{RE5}} + P_{\mathrm{RE6}} + P_{\mathrm{RE7}}) \tag{60}$$

The total driving rate of work done of Fig. 2 is obtained as:

$$P_{\mathrm{D}} = P_{\mathrm{D1}} + P_{\mathrm{D2}} + P_{\mathrm{D3}} + P_{\mathrm{D4}} + 2(P_{\mathrm{DE1}} + P_{\mathrm{DE2}} + P_{\mathrm{DE3}}) \tag{61}$$

k will be obtained by setting Eq. (60) equals Eq. (61).

NHESSD
3, 1291–1328, 2015

4 Comparison of the authors' method with other analytical solutions

Referring to Fig. 1, when $b = 0$, based on the slip-line solutions by Sokolovskii (1954), the closed-form solution N_c to the ultimate load q_u for a weightless soil mass is given by:

$$N_c = c \cdot \cot\varphi \left\{ \tan^2\left(45^\circ + \frac{\varphi}{2}\right) \exp[(\pi - 2\beta)\tan\varphi] - 1 \right\} \tag{62}$$

For a two-dimensional plane problem with weightless soil mass, N_c values for different slope angles are calculated by using of formulas (40) and (62) separately, and the results are shown in Fig. 3. The general tends for the variations of the N_c and angle friction, which was predicted by both of the methods are similar, but N_c values by Eq. (40) are only slightly larger than the N_c values by Eq. (62). This indicates that the three-dimensional failure mechanism of Fig. 1 is a reasonable upper bound solution for two-dimensional analysis.

Further comparison has been carried out for a three dimensional slope stability analyses with the following soil properties ($c = 20\,\mathrm{kN/m^2}$, $\varphi = 20^\circ$ and $\gamma = 20\,\mathrm{kN/m^3}$) and slope geometry ($B = 2\,\mathrm{m}$, $b = 1\,\mathrm{m}$, $D = 0\,\mathrm{m}$ and $H = 6\,\mathrm{m}$). The results of the dimensionless limit pressure q_u/c values with different L/B values are illustrated in Fig. 4, and the results by the authors are slightly smaller and better than those by Michalowski (1989). The ultimate pressures decrease with the increase in L/B ratio. Until the L/B value greater than 5, the normalized ultimate pressures are not sensitive to the variations of the L/B values. Such tends are shown in both of the methods. This indicates that the effect of the patched pressure on the top surface of the slope will increases rapidly as the dimension L/B ratio is reduced, especially for $L/B < 5$. Moreover, the ultimate pressures given by the authors are slightly lower than the ultimate pressure given by Michalowski (1989) which required more parameters in the formulations, and this has demonstrated that the present three-dimensional failure modes are more reasonable and more critical than that by Michalowski (1989). Compared with other previous works,

NHESSD
3, 1291–1328, 2015

the present results can give better predictions for the ultimate local pressure on the top surface of the slope.

4.1 Verification by numerical analysis

To verify the authors' analytical formulations, a series of numerical analyses are carried out. FLAC3-D finite difference package is adopted for the three-dimensional strength reduction analysis (SRM). In example 1, the soil properties parameters are $c = 20\,\mathrm{kN/m^2}$, $\varphi = 20^\circ$ and $\gamma = 20\,\mathrm{kN/m^3}$ while the geometry are given by $B = 2\,\mathrm{m}$, $b = 1\,\mathrm{m}$, $D = 0\,\mathrm{m}$, $H = 6.0\,\mathrm{m}$ and $\beta = 45^\circ$. The safety factors evaluated from the authors' analytical solution and the numerical analyses are shown in Table 1. The maximum difference between the results is less than 10 %. Both methods predicted that the safety factor k is increased as the L/B ratios decreased gradually, which is a typical illustration of the importance of three-dimensional effects. When $L/B = 1.0$, the failure surface from SRM is still a basically two-dimensional mechanism which is illustrated in Fig. 5, and the factor of safety from SRM is only 1.71 which is far from 2.084 from the present 3-D failure mechanism. Unless the loading is large enough, a distinct 3-D failure mechanism is not formed by the 3-D SRM which is a limitation of the SRM, and the present mechanism is better than the SRM in this respect. It is found that when L/B ratio is great so that the failure mechanism is approaching a two-dimensional failure, the results from Eq. (40) is virtually the same as the results from three-dimensional SRM. When L/B ratio is small, there are however more significant differences between the present failure mechanism and the SRM. The shear strain contour at the ultimate state was shown in Fig. 5. There is a high concentration of the shear strain (shear band) from the top surface of the slope which propagates towards the toe of the slope.

4.2 Verification by laboratory model tests

A laboratory test complying exactly with the present problem as shown in Fig. 6 has been conducted for the verification of the proposed method. A hydraulic jack applied a local pressure on top of a 0.8 m high 65° slope. The soil used for the model slope is classified as highly permeable poorly graded river sand. The unit weight and the relative density are $\gamma = 15.75\,\mathrm{kN/m^3}$ and 0.55 respectively. Shear strength parameters ($c' = 7$ kPa and $\varphi' = 35°$) of the soil was determined by means of consolidated drained triaxial test. The depth, breadth and height of the soil tank are 1.5, 1.85 and 1.2 m respectively. The soil is compacted by an electric compactor with a 0.2 m × 0.2 m wooden end plate. Five Linear Variable Differential Transducers (LVDT) are set up to measure the displacement of soil at different locations which are included the upper right (RHS), upper left (LHS), lower right (RHS) and lower left (LHS) are shown in Fig. 7, and the displacements at different vertical loads are monitored up to failure as shown in 8. The 2 pairs of transducers on the slope surface are placed symmetrically with a horizontal spacing of 300 mm. The first and second pairs of transducers are placed at vertical distances of 150 and 450 mm from the top of the slope respectively.

The vertical displacement controlled hydraulic jack exerts uniform distributed pressure on a 10 mm thick steel bearing plate with size $B = 0.3$ m and $L = 0.644$ m at 0.13 m away from the crest of the model ($b = 0.13$ m) until an ultimate load of 35 kN is attained at an displacement of about 6 mm as shown in Fig. 8. As a result, the ultimate bearing capacity of the slope under the current soil properties, geometrical conditions and boundary conditions is 181.2 kPa which gives a factor safety 1.021 by the present method, and this value is very close to 1.0 which demonstrates that the result is reasonable. For the slope surface, the corresponding displacement at the maximum pressure is about 2 and 1 mm at top and bottom of the slope respectively. Beyond the peak load, the applied load decreases with the increasing jack displacement. It is clear that the displacements of the slope are basically symmetrical. The failure surface of the present test is shown in Figs. 9 and 10, and the sectional view at the middle of the failure mass is shown in Fig. 11. In Fig. 8, after the maximum load is achieved, the load will decrease with increasing displacement. At this stage, the local triangular failure zone is fully developed while the failure zones at the two ends of the plate are not clearly formed. When the applied load has decreased down to about 25 kN, the load maintained constant for a while and the failure zones at the two ends are becoming visually clear. When the displacements are further increased, the applied load decreases further and the failure zone propagate towards the slope surface until the failure surface as shown in Fig. 10 is obtained. This three-dimensional failure mechanism a measured from the model test is basically similar to that as given in the present paper, and the prediction of the factor of safety from the present theory is also satisfactory.

For this test, there are several interesting phenomena worth discussing. The failure profile and cracks first initiated beneath the footing as shown in Fig. 9, which is a typical bearing capacity/slope stability failure with a triangular failure zone. This can also be observed from the upper part of the failure profile as shown in Figs. 9 and 10. ζ, ε and η are obtained as 68°, 67.5° and 83.8° from the critical factor of safety as given by Eq. (43). As the load increased, the failure zone extended and propagated towards the toe of the slope and the final failure surface is shown in Fig. 10. It is observed that the failure mechanism of the physical model test is hence a local triangular failure beneath the bearing plate, and the failure surface propagates towards the slope surface until a failure mechanism is formed. The failure profile matched reasonably well with that as predicted from the present formulation as shown in Fig. 11, and is also in compliance with that as developed by Cheng and Au (2005) using the slip line method. In addition, the prediction of the factor of safety is also close to the back analysis result of the laboratory test. In views of the difficulty in ensuring complete uniformity for the compaction of the model slope, the small discrepancy between the predicted and measured failure profiles as shown in Fig. 11 can be considered as acceptable.

5 Discussion and conclusions

Based on the upper bound theorem of limit analysis, three-dimensional slope stability problem with a patched uniform distributed load on the top surface are investigated. The authors' analytical method has demonstrated that the present failure mechanisms are reasonable in predicting the bearing capacity under a patched load on the top

NHESSD
3, 1291–1328, 2015

surface of slope which is commonly found for bridge abutment foundation. Furthermore, combined with the traditional safety factor k, the allowable load on the top surface of the slope can be obtained by a simple looping method (using Excel or any computer language). The search for the critical factor of safety is just several seconds which is much faster than that by the SRM which requires about half to 1 day for a complete analysis (and about half a day to set up the computer model for an experienced user), but the results from the proposed analysis is very close to that from the tedious analysis using SRM.

The present formulations are the further extension of previous works, with slightly improved results and more versatile for both surface patch load or buried patch load. Based on the model test and the SRM analysis, it is clear that the present work can be used by engineers for routine analysis and design, and it can provide fast and reliable solution suitable for many practical problems.

The present problem can be viewed as a bearing capacity as well as a slope stability problem, as both types of problem are governed by the same yield and equilibrium requirements. The laboratory test has demonstrated that the present formulation is reasonable, and it will actually reduce to the classical Prandtl mechanism when $\beta = 0$. The accuracy and suitability of the present formulation are hence also justified from theoretical point of view.

Acknowledgements. The authors would like to thanks to the support from The Hong Kong Polytechnic University through the account ZVCR and Research Grant Council project PolyU 5128/13E.

Appendix A: Notation

A Discontinuity area dominant

B Width of the footing

b Distance away from the crest of slope for the patched load

c Soil cohesion strength

c_e Mobilized cohesive strength

D Embedment depth

H Height of slope

k Safety factor

L Load length

N_c Bearing capacity factor

q External pressure

q_u Ultimate bearing pressure

V Volume domain

S Boundary area domain

P_{R} Resistance rate of work done

P_{D} Driving rate work done

φ Internal friction angle

φ_e Mobilized internal friction angle

$f(\sigma_{ij})$ Yield function

β Slope angle

$\dot{\varepsilon}_{ij}$ Strain rate tensors

λ Non-negative scalar function

NHESSD
3, 1291–1328, 2015

Title Page
Abstract Introduction
Conclusions References
Tables Figures
Back Close
Full Screen / Esc
Printer-friendly Version
Interactive Discussion

η, ξ, θ, ε, Θ Angle of the wedges as shown in Fig. 1

η_{cr}, ξ_{cr} Angle of the wedge at failure as shown in Fig. 1

σ_{ij} Stress tensors

t_i Tractions over the velocity jumps $[v]_i$

$[v]_i$ Velocity jumps

γ_i Unit weight

v_0, v_3 Velocity along the failure profile as shown in Fig. 1

v_1 Velocity of the patched load

x, y, z Coordinates of the slope surface or the failure profile

References

Azzouz, A. S. and Baligh, M. M.: Loaded areas on cohesive slopes, J. Geotech. Eng.-ASCE, 109, 709–729, 1983.

Bagge, G.: Tension cracks in saturated clay cutting, in: Proceedings of the 11th International Conference on Soil Mechanics and Foundation Engineering, 12–16 August, San Francisco, 393–395, 1985.

Baker, R.: Tensile strength, tensile cracks, and stability of slopes, Soils Found., 21, 1–17, 1981.

Bishop, A. W.: The use of the slip circle in stability analysis of slopes, Geotechnique, 5, 7–17, 1955.

Chen, J., Yin, J. H., and Lee, C. F.: Upper bound limit analysis of slope stability using rigid elements and nonlinear programming, Can. Geotech. J., 40, 742–752, 2003.

Chen, R. H. and Chameau, J. L.: Three dimensional limit equilibrium analysis of slopes, Geotechnique, 32, 31–40, 1982.

Chen, W. F.: Limit analysis and soil plasticity, Elsevier Scientific Publishing Company, USA, 47–106, 1975.

Chen, W. F.: Limit analysis in soil mechanics, Elsevier Scientific Publishing Company, USA, 437–469, 1990.
Chen, Z., Wang, X., Haberfield, C., Yin, J. H., and Wang, Y.: A three dimensional slope stability analysis method using the upper bound theorem, Part 1: Theory and methods, Int. J. Rock Mech. Min., 38, 369–378, 2001a.
Chen, Z., Wang, J., Wang, Y., Yin, J. H., and Haberfield, C.: A three dimensional slope stability analysis method using the upper bound theorem, Part 2: numerical approaches, applications and extensions, Int. J. Rock Mech. Min., 38, 379–397, 2001b.
Cheng, Y. M. and Au, S. K: Slip line solution of bearing capacity problems with inclined ground, Can. Geotech. J., 42, 1232–1241, 2005
Cheng, Y. M. and Yip, C. J.: Three-dimensional asymmetrical slope stability analysis – extension of Bishop's and Janbu's techniques, J. Geotech. Geoenviron. Eng.-ASCE, 133, 1544–1555, 2007.
Cheng, Y. M., Lansivarra, T., and Wei, W. B.: Two-dimensional slope stability analysis by limit equilibrium and strength reduction methods, Comput. Geotech., 34, 137–150, 2007.
Cheng, Y. M., Lansivaara, T., Baker, R., and Li, N.: The use of internal and external variables and extremum principle in limit equilibrium formulations with application to bearing capacity and slope stability problems, Soils Found., 53, 130–143, 2013.
Das, B. M.: Theoretical foundational engineering, Elsevier Scientific Publishing Company, USA, 413–416, 1987.
Farzaneh, O. and Askari, F.: Three-dimensional analysis of nonhomogeneous slopes, J. Geotech. Geoenviron., 129, 137–145, 2003.
Gens, A., Hutchinson, J. N., and Cavounidis, S.: Three dimensional analysis of slides in cohesive soils, Geotechnique, 38, 1–23, 1988.
Giger, M. W. and Krizek, R. J.: Stability analysis of vertical cut with variable corner angle, Soils Found., 15, 63–71, 1975.
Gunnar, B.: Tension cracks in saturated clay cuttings, in: Proceedings of the 11th International Conference on Soil Mechanics and Foundation Engineering (II), 12–16 August, Rotterdam, edited by: Balkema A. A., 442–446, 1985.
Hovland, H. J.: Three dimensional slope stability analysis method, J. Geotech. Eng.-ASCE, 103, 971–986, 1977.
Hungr, O.: An extension of Bishop's simplified method of slope stability analysis to three dimensions, Geotechnique, 37, 113–117, 1987.

NHESSD
3, 1291–1328, 2015

Huang, C. C. and Tsai, C. C.: New method for 3-D and asymmetrical slope stability analysis, J. Geotech. Geoenviron., 126, 917–927, 2000.
Huang, C. C. and Tsai, C.C.: General method for three-dimensional slope stability analysis, J. Geotech. Geoenviron., 128, 836–848, 2002.
Lam, L. and Fredlund, D. G.: A general limit equilibrium model for three-dimensional slope stability analysis, Can. Geotech. J., 30, 905–919, 1993.
Michalowski, R. L.: Three dimensional analysis of locally loaded slopes, Geotechnique, 39, 27–38, 1989.
Morgenstern, N. R. and Price, V. E.: The analysis of stability of general slip surfaces, Geotechnique, 15, 79–93, 1965.
Spencer, E.: A method of analysis of the stability of embankments assuming parallel inter-slice forces, Geotechnique, 17, 11–26, 1967.
Wei, W. B., Cheng, Y. M., and Li, L.: Three-dimensional slope failure by strength reduction and limit equilibrium methods, Comput. Geotech., 36, 70–80, 2009.

Table 1. Safety factors and geometric parameters (Example 1 and geometry of failure mass) for $q = 100$ kPa.

k	ζ_{cr}	ξ_{cr}	η_{cr}	h (m)	cc' (m)	gg' (m)	ii' (m)	L/B	k from SRM
1.120	69.0	68.3	94.75	6.00	0.88	3.51	0.21	∞	1.19
1.278	67.8	67.1	97.75	6.00	0.74	3.08	0.18	10	1.26
1.311	67.3	67.0	98.25	6.00	0.72	3.01	0.17	8	1.30
1.368	67.0	66.8	99.25	6.00	0.67	2.88	0.16	6	1.33
1.466	64.6	64.3	97.75	4.97	0.57	2.30	0.16	4	1.41
1.706	60.8	60.5	95.00	3.72	0.43	1.57	0.15	2	1.60
2.080	57.0	56.8	92.00	2.83	0.32	1.05	0.14	1	1.71

NHESSD
3, 1291–1328, 2015

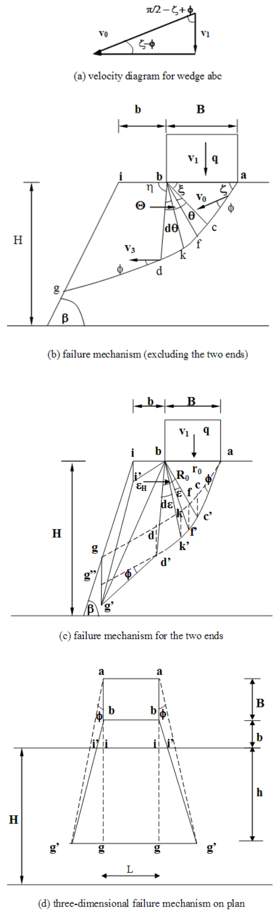

Figure 1. Three-dimensional failure mechanism for slope problem with a patch load.

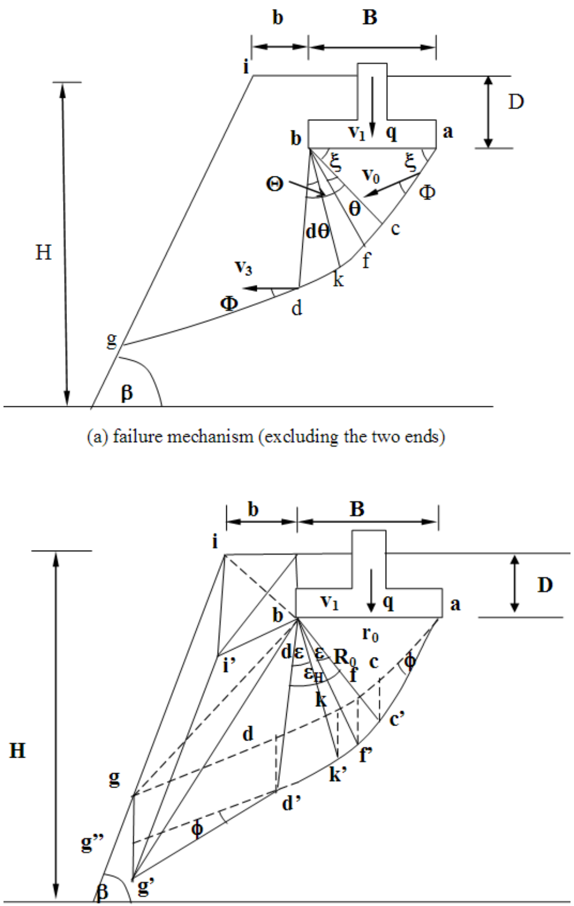

(a) failure mechanism (excluding the two ends)

(b) failure mechanism for the two ends

Figure 2. Three-dimensional failure mechanism for slope with buried patch load.

NHESSD

3, 1291–1328, 2015

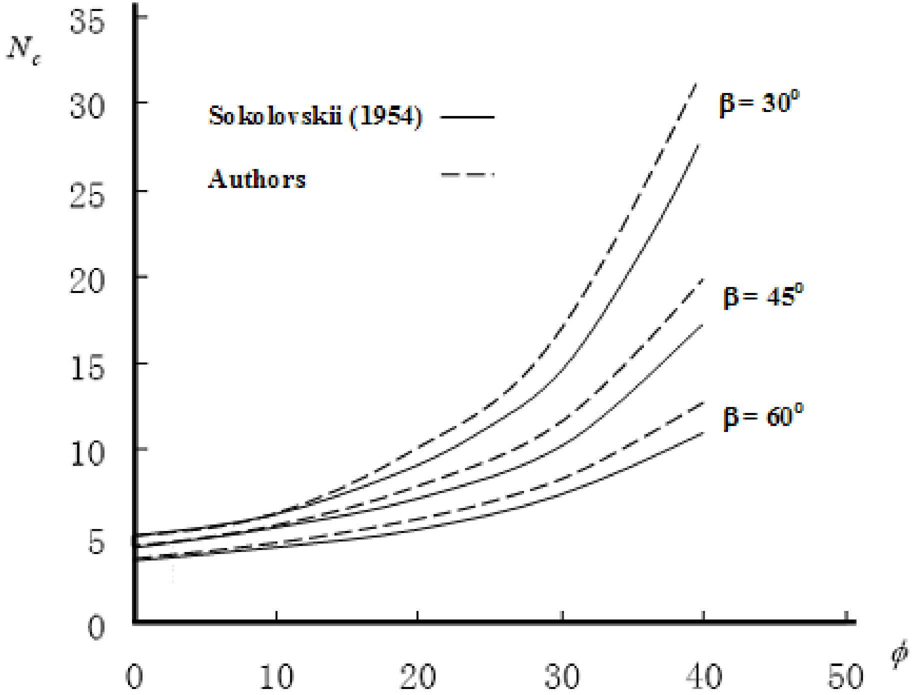

Figure 3. Comparison of N_c values between Sokolovskii method and authors' method.

NHESSD
3, 1291–1328, 2015

Three dimensional slope stability problem

Y. M. Cheng et al.

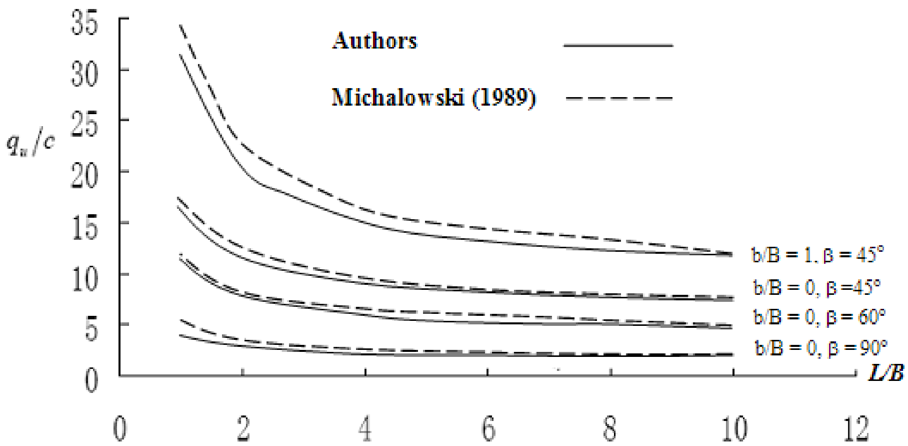

Figure 4. Comparison of present results with upper-bound solutions by Michalowski (1989).

NHESSD
3, 1291–1328, 2015

Three dimensional slope stability problem

Y. M. Cheng et al.

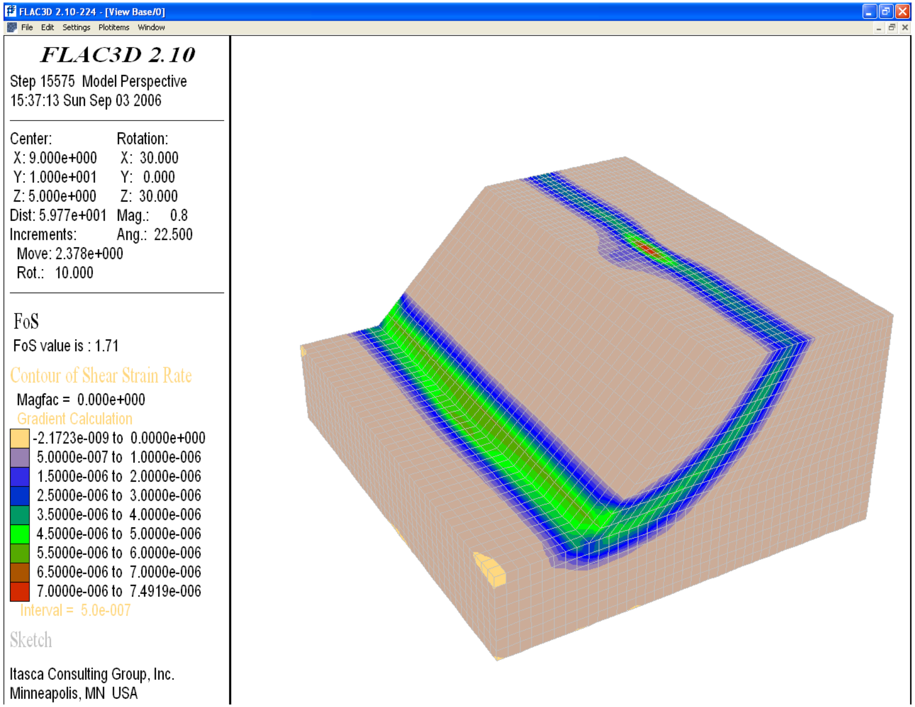

Figure 5. Failure mechanism for $L/B = 1.0$ by SRM (shear strain distribution).

Figure 6. Basic setup of the laboratory test.

NHESSD

3, 1291–1328, 2015

Three dimensional slope stability problem

Y. M. Cheng et al.

Figure 7. LVDT at top and sloping face of the model test.

NHESSD
3, 1291–1328, 2015

NHESSD

3, 1291–1328, 2015

Three dimensional slope stability problem

Y. M. Cheng et al.

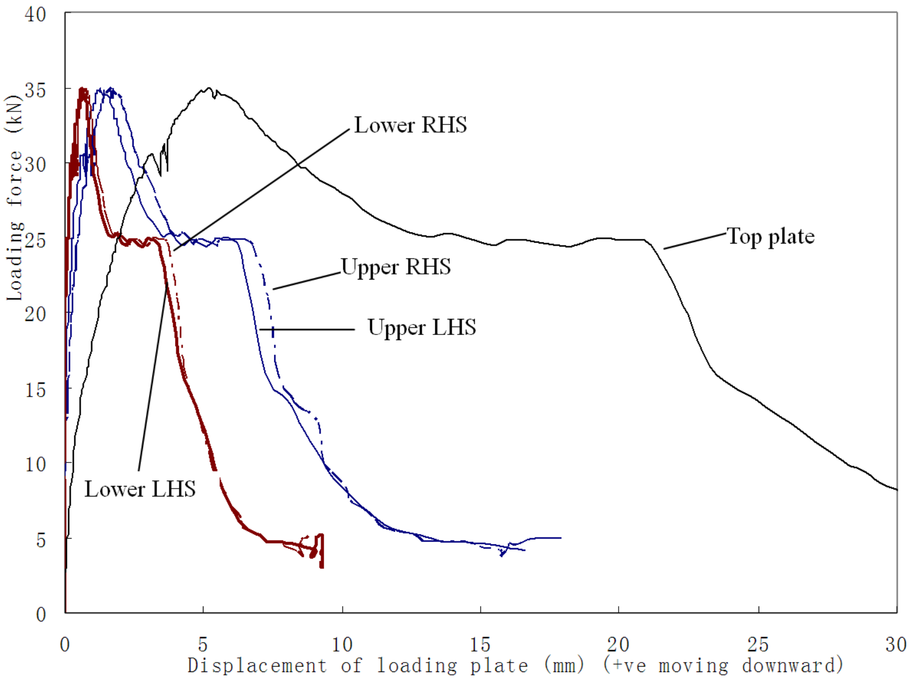

Figure 8. Loading force against the displacement of slope surface.

Figure 9. Slope failure beneath bearing plate.

Figure 10. Global three-dimensional slope failure.

NHESSD
3, 1291–1328, 2015

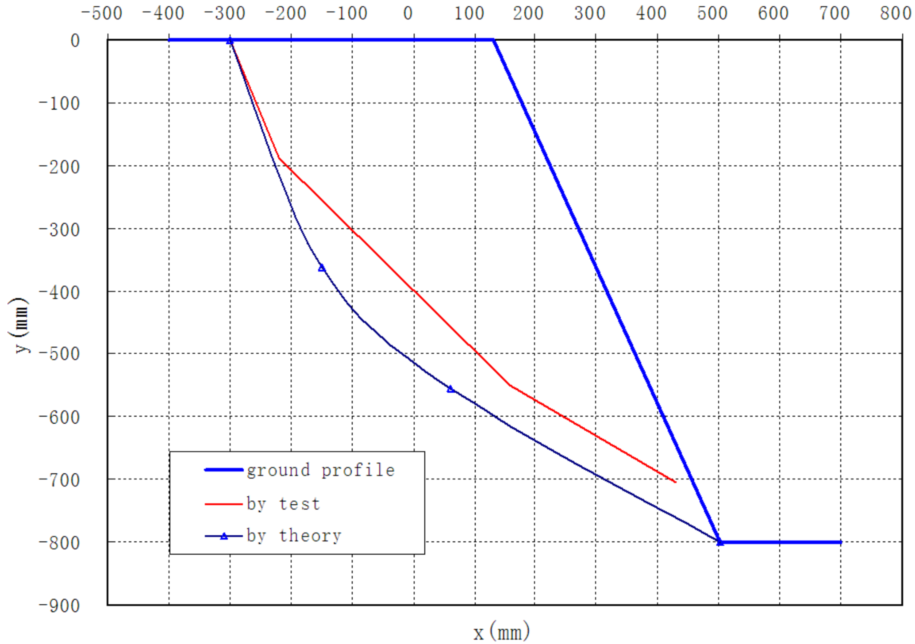

Figure 11. Comparisons between the measure and the predicted failure surface profile at mid-section of failure.